

Aerosols and tides in the martian tropics during southern hemisphere spring equinox from Mars Climate Sounder data

L. J. Steele, A. Kleinböhl, D. M. Kass and R. W. Zurek

Jet Propulsion Laboratory, California Institute of Technology, Pasadena, California, USA.

Corresponding author: Liam Steele (liam.j.steele@jpl.nasa.gov)

Key points

- Mars year 29 has large amplitude thermal tides in the tropics during southern hemisphere spring equinox that are not seen in other years.
- Data in other years suggests there was a shift in the phase of the diurnal tide to an earlier local time in MY29, due to early dust activity.
- Radiative cooling from water ice clouds at night causes increased downwelling and stronger temperature inversions due to adiabatic warming.

arXiv:2011.08996v1 [astro-ph.EP] 17 Nov 2020

Abstract

We analyze Mars Climate Sounder temperature and aerosol data in the tropics to study atmospheric tides and their relation to the dust and water ice distributions. Our results from data covering Mars years (MY) 29–35 reveal that MY29 has large amplitude non-migrating thermal tides during southern hemisphere spring equinox that are not observed at the same local time in any other year. It is the nighttime temperatures that are most perturbed compared to other years, with strong temperature inversions at 35–55 km altitude. Analysis of data at different local times reveals that the temperatures and water ice clouds at 03:45 am in MY29 more closely resemble those at 05:00 am in other years, suggesting there was a shift in the phase of the diurnal tide to an earlier local time. This phase shift, and the large amplitude non-migrating thermal tides, appear to be related to early dust activity. Two early dust storms occurred in MY29 around the time there was upwelling over the tropics, associated with the Hadley circulation, enabling the dust to be transported to higher altitudes where it has a larger radiative influence. As well as dust, water ice clouds are also found to influence the tidal structure. Due to the interaction of non-migrating tides, water ice clouds occur in two discrete longitudinal regions at night. The increased radiative cooling results in increased downwelling above the clouds, leading to increased adiabatic warming and a strengthening the temperature inversions.

Plain Language Summary

Tides can cause oscillations in Mars' atmosphere, just like they can cause oscillations in the Earth's oceans. The tides on Mars are caused by variations in the heating of the atmosphere by the sun, and they can affect temperatures, wind, pressure, and the transport of aerosols. We investigate these tides using data from the Mars Climate Sounder instrument onboard the Mars Reconnaissance Orbiter spacecraft. We find that while the daytime atmosphere in different years is similar, the nighttime atmosphere in one particular year - Mars year 29 - has a noticeably different structure. We determine that this difference is due to a combination of the effects of both dust and water ice. These aerosols cause regions of localized heating and cooling, which affects the structure of the tides, and the circulation of the atmosphere.

1 Introduction

Thermal tides are global-scale oscillations of atmospheric temperature, pressure and wind, which are sub-harmonics of a solar day. They are driven by solar heating of the atmosphere and surface, and due to Mars' thinner atmosphere they play a much more significant role than on Earth. They can influence surface pressure and wind, affect the transport of aerosols, and propagate into the upper atmosphere (Zurek, 1976; Wilson and Hamilton, 1996; Forbes, 2002). Observations of thermal tides on Mars date back to the 1970s, when data from Mariner 9 and the Viking landers and orbiters were analyzed (e.g. Leovy et al., 1973; Zurek, 1976, 1988; Conrath, 1976; Leovy and Zurek, 1979; Leovy, 1981; Wilson and Richardson, 2000). Since this time, orbiters and surface instruments have provided a wealth of data about the tides.

Data from the Rover Environmental Monitoring Station (REMS) on board the Mars Science Laboratory (MSL) are the most complete set of surface data since the Viking landers. MSL is located near the equator within Gale crater, and the tropics are a region with weather dominated by tides (Wilson and Hamilton, 1996; Hinson and Wilson, 2004; Hinson et al., 2008). REMS measurements show that diurnal and semidiurnal tides in Gale Crater are highly correlated with atmospheric opacity, with enhanced tidal amplitudes observed during the Mars Year (MY) 34 dust storm (Guzewich et al., 2016, 2019; Viúdez-Moreiras et al., 2019).

Vertical profiles of global atmospheric temperatures in the lower and middle atmosphere (at altitudes below ~ 80 km), particularly from the Thermal Emission Spectrometer (TES) and Mars Climate Sounder (MCS) instruments, provide a rich data set with which to analyze thermal tides. Such data, covering multiple Mars years, have revealed the presence of migrating (sun-synchronous) tides, as well as non-migrating tides that can move westward or eastward, with zonal wavenumbers of 1–4 being most prominent (Banfield et al., 2000, 2003; Lee et al., 2009; Guzewich et al., 2012; Kleinböhl et al., 2013; Guzewich et al., 2014; Wu et al., 2015, 2017). Thermal tides have also been detected in the thermosphere, with analysis of accelerometer data from the aerobraking phases of Mars Global Surveyor and Mars Odyssey revealing zonal wavenumber 2–3 patterns in density at altitudes of 100–160 km (Keating et al., 1998; Withers et al., 2003; Wang et al., 2006). More recently, Mars Atmosphere and Volatile Evolution (MAVEN) measurements have been used to detect zonal wavenumber 1–3 structures at altitudes of up to 190 km (Lo et al., 2015; England et al., 2016; Stevens et al., 2017; Jiang et al., 2019). MGS Radio Science measurements have revealed tidal effects up to altitudes of 200 km (Bougher et al., 2004; Cahoy et al., 2006), while Mars Reconnaissance Orbiter (MRO) radio tracking data have revealed zonal wavenumber 1–2 patterns in density in the exosphere, at ~ 250 km (Mazarico et al., 2008).

Numerical simulations and classical tidal theory suggest that the zonal patterns observed in the atmosphere are the result of thermal tides propagating from at or near the surface. These tides are modulated by variations in Mars' surface properties (topography, thermal inertia and albedo), the atmospheric dust loading, water ice clouds, and interactions between planetary waves and tides (Zurek, 1976; Conrath, 1976; Joshi et al., 2000; Forbes and Hagan, 2000; Wilson, 2002; Hinson and Wilson, 2004; Forbes and Miyahara, 2006; Moulden and Forbes, 2008a,b, 2010, 2011). Eastward-propagating Kelvin waves are found to be the dominant component for zonal wavenumbers > 1 (Wilson, 2000; Banfield et al., 2003; Withers et al., 2011; Guzewich et al., 2012), as these are close to resonance in the martian atmosphere (Zurek, 1988; Wilson and Hamilton, 1996).

For global temperature data from low polar orbiters, available at two local times 12 hours apart (~ 2 am/pm for TES data and ~ 3 am/pm for MCS in-track data), the standard tidal analysis technique is to perform Fourier analysis of the average and difference fields of the two local times (e.g. [Banfield et al., 2003](#); [Lee et al., 2009](#); [Guzewich et al., 2012](#)). To date, studies utilizing MCS data have only performed Fourier analysis on the in-track measurements, observed in the direction of MRO’s orbital movement. MCS also performed cross-track scanning, viewing the limb at 90° to the left and right of the orbit trajectory, obtaining measurements between 1.5–3 hours earlier and later in local time than the in-track measurements, depending on latitude. [Kleinböhl et al. \(2013\)](#) used the cross-track data to study tides by applying nonlinear least-squares fits to the time series data, but Fourier analysis of the data, and investigations of the aerosol behavior, have not been performed. We perform this additional analysis here, in order to investigate the temporal behavior of thermal tides and their relation to aerosols. In particular, we focus our attention on the tropics, as this region was not analyzed in earlier studies.

2 Data and analysis method

MCS is a nine-channel limb radiometer on board MRO, with 8 mid- and far-infrared (IR) channels and one visible/near-IR channel. Each channel consists of 21 detectors, providing a radiance profile from the surface to ~ 90 km, with ~ 5 km resolution ([McCleese et al., 2007](#)). The retrieval algorithm inverts the radiance profiles to produce geophysical quantities, including vertical profiles of temperature, dust and water ice extinction ([Kleinböhl et al., 2009, 2011, 2017](#)). MCS typically observes the limb in the direction of MRO’s orbital movement, producing in-track measurements. However, beginning in MY30, and continuing through MY35, the observation strategy was modified to also view the limb at 90° to the orbit trajectory, producing cross-track measurements ([Kleinböhl et al., 2013](#)). [Figure 1](#) shows how the local times of the measurements vary with latitude. As the orbit moves from the equator to $\pm 60^\circ$ latitude, the time spanned by the earlier (blue) and later (red) cross-track measurements increases from ~ 2.7 hours to ~ 6.2 hours. For simplicity, and due to focusing on the tropics, when referring to local times we will reference the equator-crossing local time.

In order to perform Fourier analysis on the MCS temperature retrievals, we first binned the data spatially and temporally on the MCS retrieval pressure levels. We binned the data by 15° in longitude, 5° in latitude and 5° in L_S . These values were chosen to ensure the majority of bins were filled with data, but that bins were not too large that potentially interesting spatial and temporal structures were missed. As Fourier analysis requires all longitudinal bins at a given latitude and pressure level to be populated, bins with missing data were filled using cubic spline interpolation. Interpolation was not performed if two consecutive longitudes bins had missing data, or if more than 25% of the longitudinal bins had missing data. For the period we are interested in ($L_S \approx 180\text{--}360^\circ$) there are typically one or two longitudinal bins in the tropics during the day-time that require interpolation. Away from the tropics, and at most locations during the night, interpolation is typically not required.

For the in-track data (green symbols in [Figure 1](#)), and the cross-track data at earlier and later local times (blue and red symbols in [Figure 1](#)), binning produced morning (am) and afternoon (pm) temperature fields, from which averages and differences were created via:

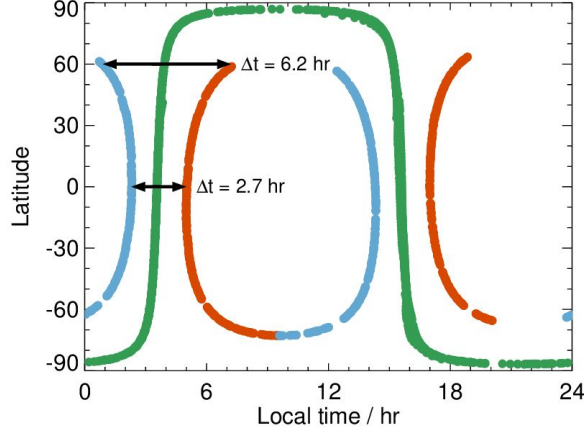


Figure 1: Local time coverage of MCS in-track (green) and cross-track (blue, red) measurements. Data are from MY30, $L_S = 185\text{--}190^\circ$.

$$T_{\text{ave}} = (T_{\text{pm}} + T_{\text{am}})/2, \quad (1)$$

$$T_{\text{diff}} = (T_{\text{pm}} - T_{\text{am}})/2. \quad (2)$$

For periods with only in-track data this resulted in one T_{ave} and one T_{diff} field, while for periods with in-track and cross-track data there were three T_{ave} and three T_{diff} fields. Fourier analysis was then performed, in order to obtain the amplitudes and phases of the tides. This assumes that at a given latitude and pressure level, the temperature variation with longitude, λ , and local time, t_{LT} , can be expressed as

$$\begin{aligned} T(\lambda, t_{\text{LT}}) &= \sum_{s,\sigma} T_{s,\sigma} \cos[(s - \sigma)\lambda + \sigma t_{\text{LT}} - \delta_{s,\sigma}] \\ &= \sum_{s,\sigma} T_{s,\sigma} \cos(m\lambda + \sigma t_{\text{LT}} - \delta_{s,\sigma}), \end{aligned} \quad (3)$$

where $s = 0, \pm 1, \pm 2, \dots$ is the zonal wavenumber (with positive and negative values denoting westward and eastward propagation respectively), $\sigma = 0, 1, 2, \dots$ is the frequency, $m = |s - \sigma|$ is the satellite-relative wavenumber, $T_{s,\sigma}$ is the amplitude of the tide and $\delta_{s,\sigma}$ is the phase. A stationary wave has $\sigma = 0$, while diurnal and semidiurnal tides have $\sigma = 1$ and $\sigma = 2$, respectively. Fourier analysis of T_{ave} and T_{diff} provides different information on the tides present. For example, only even (odd) values of σ appear in the T_{ave} (T_{diff}) fields. Some thermal tides can propagate vertically in the atmosphere, while others are trapped in the region of excitation. Additionally, thermal tides can be decomposed into components which are symmetric or anti-symmetric about the equator. (For more details see [Forbes, 1995](#); [Banfield et al., 2003](#); [Lee et al., 2009](#); [Guzewich et al., 2012, 2014](#).)

When discussing various tidal components we will use ‘D’ and ‘S’ to denote diurnal and semidiurnal tides, and ‘E’ and ‘W’ to denote eastward and westward propagation, with the number following denoting the zonal wavenumber s . For example, DE1 represents an eastward-propagating diurnal wavenumber 1

tide, while SW2 denotes a westward-propagating semidiurnal wavenumber 2 tide. Zonally-symmetric tides, which do not propagate eastward or westward and have no zonal wavenumber, are represented by D0 or S0. Tides which propagate westward with the apparent phase speed of the Sun (e.g. DW1 and SW2) are called migrating tides, while the others are called non-migrating.

3 Results

3.1 Tide amplitudes

We first look at the amplitudes from the Fourier analysis of the T_{ave} and T_{diff} fields. We focus on satellite-relative wavenumbers $m = 1-3$, as these have the largest amplitudes in the MCS data. After analyzing tides from different Mars years, it is clear that the behavior in the tropics in MY29 around southern hemisphere spring equinox ($L_S \approx 160-200^\circ$) is different to other years, and is noticeable for the appearance of tides with amplitudes > 5 K. The atmosphere around this time in MY29 was dustier than in other years observed by MCS due to two early local dust storms (Wang and Richardson, 2015). One storm originated in the northern hemisphere at $L_S \approx 143^\circ$, while another originated in the southern hemisphere at $L_S \approx 152^\circ$.

Figure 2 shows the $m = 1-3$ components of the T_{ave} and T_{diff} fields for MY29, with the data averaged over $L_S = 180-200^\circ$, which is when the amplitudes in the tropics are at their largest. The black contours overlain on the T_{ave} and T_{diff} fields show the $m = 0$ components. For T_{ave} this component is mostly dominated by the time- and zonal-mean temperature (for which $s = \sigma = 0$), but will also have contributions from the sun-synchronous semidiurnal tide, SW2, and possibly higher even-harmonic sun-synchronous tides. For T_{diff} this component is mostly dominated by the sun-synchronous diurnal tide, DW1, with additional contributions from higher odd-harmonic sun-synchronous tides (Zurek, 1976; Banfield et al., 2003; Lee et al., 2009; Guzewich et al., 2012; Kleinböhl et al., 2013).

The tidal features in the mid- to high- latitudes have been discussed in detail previously (Wilson and Hamilton, 1996; Banfield et al., 2000, 2003; Lee et al., 2009; Guzewich et al., 2012) so are not considered further here. Instead we focus on tides in the tropics. In the T_{ave} fields (Figure 2a-c), the regions of large amplitude tropical tides are located between $\sim 1-5$ Pa. As m progresses from 1-3, the vertical extents of these regions increase, and they shift southwards in latitude, becoming centered on the equator. In the T_{diff} fields (Figure 2d-f) the large amplitudes all occur at a similar height, centered at ~ 3 Pa, which corresponds to a region of strong gradients in the diurnal tide (black contours). They are offset north of the equator with relatively small vertical extents, and the amplitudes decrease with increasing m . For $m = 2$ and $m = 3$ in both the T_{ave} and T_{diff} fields there are two weaker tidal signatures below the main ones identified, at ~ 25 Pa and ~ 300 Pa, which are centered more on the equator.

Such large-amplitude tropical tides are not seen in the in-track measurements in other Mars years (see Figure S1), but some similar tidal features do appear when looking at cross-track measurements taken ~ 1.5 hours later in local time. Figure 3 shows the $m = 1-3$ components of the T_{ave} and T_{diff} fields from MY30 cross-track measurements at local times $\sim 5:00$ am/pm. MY30 was chosen for comparison as it is representative of the behavior seen in MY31-33 and MY35 in this L_S period (MY34 experienced a global dust storm around this time, so cannot be compared, e.g. Kass et al., 2019; Kleinböhl et al., 2020). Large amplitude

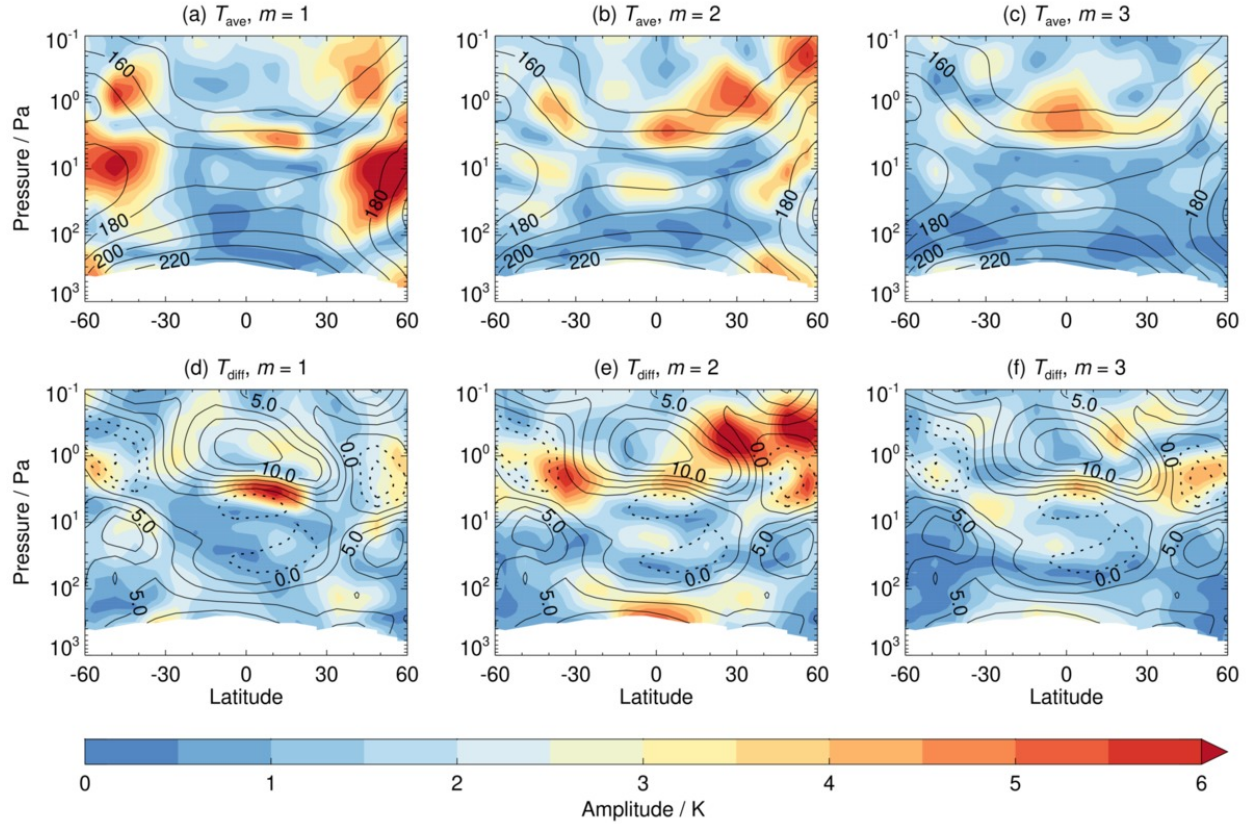


Figure 2: Amplitudes of the $m = 1-3$ components of the (a–c) T_{ave} , and (d–f) T_{diff} fields, averaged over $L_S = 180-200^\circ$, MY29. Black contours show the $m = 0$ component (10 K intervals for T_{ave} and 2.5 K intervals for T_{diff}), with dashed lines representing negative values. Data are from in-track measurements at a local time of 3:45 am/pm.

tropical tides of 4–6 K appear at this later local time in the $m = 2$ and $m = 3$ components of T_{ave} (Figure 3b,c), and a smaller amplitude tide of 2–3 K appears in the $m = 1$ component of T_{diff} (Figure 3d). These tides appear in similar locations to those seen in the MY29 in-track measurements, with again the T_{ave} amplitudes more vertically-extensive, and the T_{diff} amplitude located in the region of strong gradients in the diurnal tide.

As the tide amplitudes in the Fourier analysis are derived from daytime and nighttime temperature measurements, we can also look at these two times of day individually. The temperature distributions in the daytime are broadly similar in MY29 and MY30 (see Figure S2), but the nighttime temperature distributions are markedly different in MY29 compared to MY30. Thus, it is the nighttime temperature structure which is responsible for the large amplitude tides seen in the MY29 in-track data, and not in the MY30 in-track data. Figure 4 shows the temperature and water ice cloud distributions, as a function of longitude and altitude, from MY29 data at a local time of 03:45 am, and MY30 data at three different local times (02:20 am, 03:35 am and 05:00 am). Data are averaged between $0-10^\circ\text{N}$, as this latitude range contains large amplitudes for all tidal components in MY29. Comparing the in-track data in both years, it is clear that MY29 has prominent temperature inversions at 03:45 am between $\sim 3-20$ Pa (Figure 4d) which are not seen at 03:35

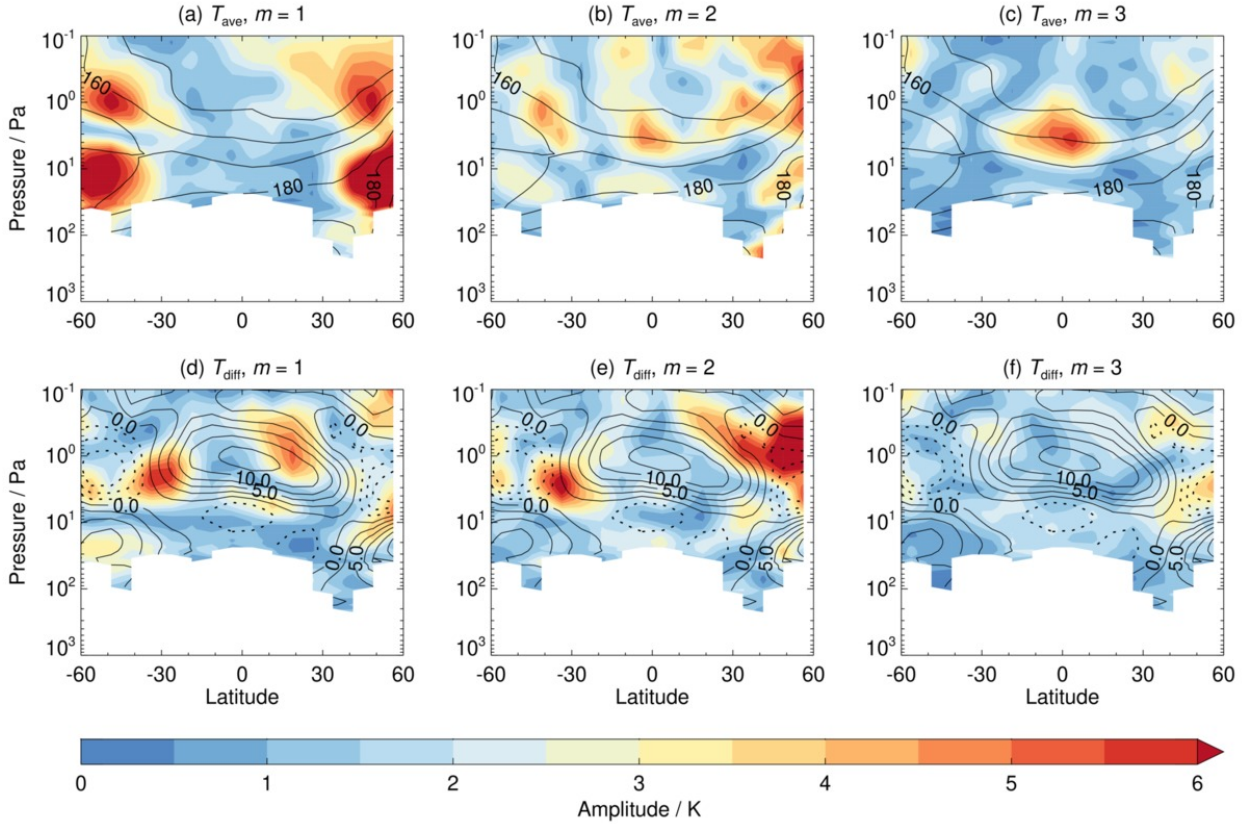


Figure 3: As Figure 2, but from MY30 cross-track measurements at a local time of 5:00 am/pm.

am in MY30 (Figure 4b). The inversions are located between 15–90°W and 75–110°E, with the inversions being strongest in the western hemisphere, where temperatures at 4 Pa are ~ 30 K warmer than in MY30. However, when looking at a later local time of 05:00 am in MY30 (Figure 4c), temperature inversions can be seen, and this results in the appearance of the tropical tide signals seen in Figure 3. As the temperature inversions in MY30 are not as strong as in MY29, and the tropical tide amplitudes are weaker.

3.2 Tide structure

3.2.1 MY30 in-track data

To further investigate the differences between the tides in MY29 and MY30, and the changes to the tides with local time in MY30, we look at the longitudinal structure of the tides, in terms of their amplitudes and phases. We begin with the tide structure from the MY30 in-track measurements, as this is similar to all years other than MY29, and so is representative of the general behavior. Figure 5 shows the $m = 1-3$ components of the amplitudes and phases of the T_{ave} and T_{diff} fields, averaged between 0–10°N and $L_S = 180-200^\circ$. Corresponding nighttime temperature and water ice distributions are shown in Figure 4b. Stationary waves and semidiurnal tides are the most likely contributors to the T_{ave} field, while diurnal tides are the most likely contributors to the T_{diff} field. Higher frequency tides (e.g. terdiurnal and quadiurnal) can also potentially

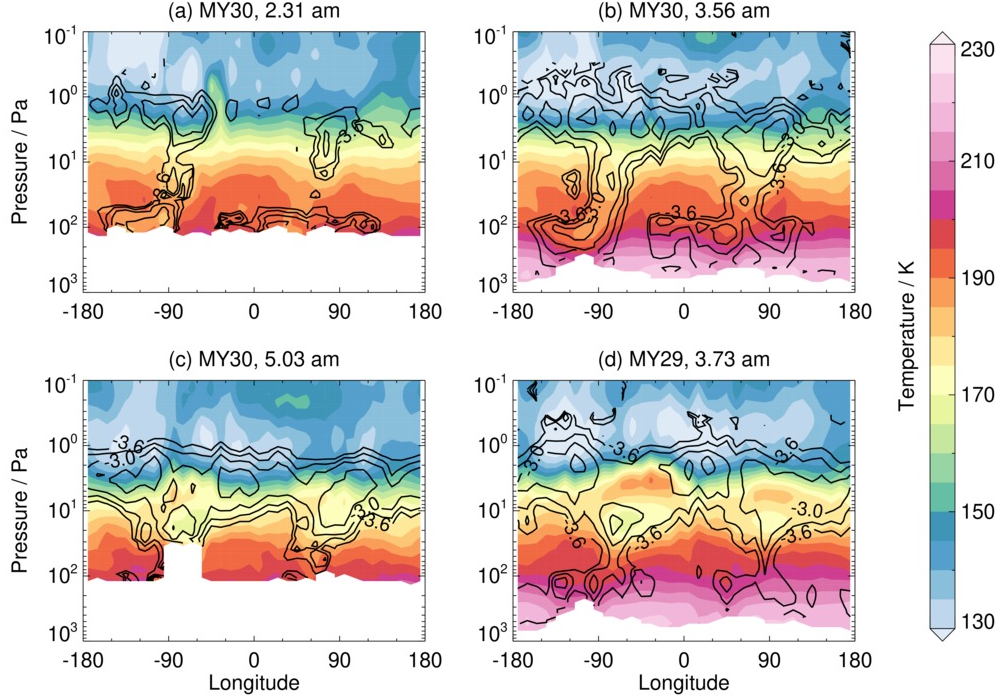


Figure 4: Temperatures (shaded) and the log of the water ice opacity per km (contours) from (a–c) MY30 in-track and cross-track data at different local times, and (d) MY29 in-track data. Ice opacity contours range from -3.6 to -2.4 , in steps of 0.3 . Data are averaged between $0\text{--}10^\circ\text{N}$ and $L_S = 180\text{--}200^\circ$. (See Figure S3 for a similar plot of the shaded water ice cloud distribution.)

contribute, though these generally have smaller amplitudes and a less significant impact on the observed tidal structure (Lee et al., 2009; Moudden and Forbes, 2014; Guzewich et al., 2016).

In terms of the T_{diff} field, the structure of the $m = 1$ component (Figure 5d) shows evidence for the zonally-symmetric diurnal tide, D0, caused by the higher altitude topography of the Tharsis region. The weak amplitudes and phase shift between $\sim 4\text{--}50$ Pa are due to the effects of the diurnal tide. This can be seen in Figure S1d, where the $m = 0$ component of T_{diff} changes sign, signifying warmer temperatures at 3:30 am compared to 3:30 pm. Outside of the tropics, where the diurnal tide behavior changes and the amplitude of the $s = 1$ component of topography increases, the D0 tide becomes stronger and extends up to ~ 10 Pa. There is also evidence of a westward-tilted tide, which is most likely DW2. This becomes more prominent at latitudes polewards of $\sim 30^\circ\text{N}$ (not shown), in tandem with the increasing amplitude of the $s = 1$ component of topography.

The $m = 2$ component of T_{diff} (Figure 5e) shows evidence of a tide with a long vertical wavelength that is tilted slightly eastward with height, which is suggestive of the DE1 tide forced by the interaction of the diurnal tide with the $s = 2$ component of topography. (This tide is most clear in MY33; see Figure S4e.) The DE1 tide has been studied extensively from the surface to the upper atmosphere, with the earliest observations revealing its presence during the 1971 global dust storm (Conrath, 1976), and an enhancement in the surface pressure signal in the Viking lander data during the 1977 global dust storms (Leovy, 1981;

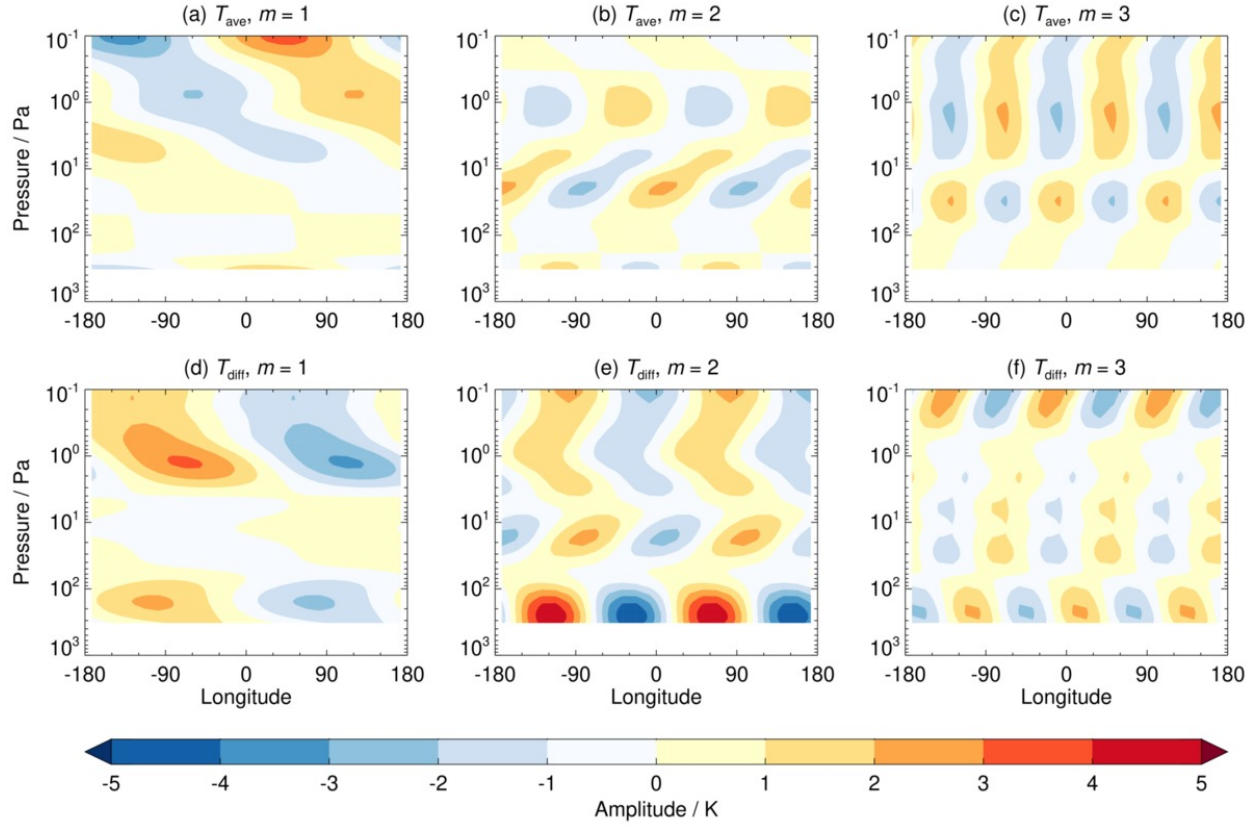


Figure 5: Amplitude and phase of the $m = 1$ – 3 components of the (a–c) T_{ave} , and (d–f) T_{diff} fields. Data are from MY30 in-track measurements at a local time of 3:30 am/pm, averaged between 0 – 10°N and $L_S = 180$ – 200° .

Zurek and Leovy, 1981; Zurek, 1988; Wilson and Hamilton, 1996; Bridger and Murphy, 1998). Analysis of orbiter data and computer simulations have also revealed the presence of DE1 in the lower and middle atmosphere (Wilson and Hamilton, 1996; Wilson, 2000; Banfield et al., 2000, 2003; Hinson et al., 2008; Guzewich et al., 2012, 2014) as well as its dominance high in the atmosphere (Wilson, 2002; Wang et al., 2006; Withers et al., 2011; Lo et al., 2015).

The $m = 3$ component of T_{diff} (Figure 5f) shows evidence for an eastward propagating tide with a long vertical wavelength, which is most likely DE2. There have been numerous studies of DE2, from the lower atmosphere up to aerobraking altitudes where it is found to play a prominent role in the density structure (Wilson, 2000, 2002; Banfield et al., 2003; Wang et al., 2006; Withers et al., 2011; Guzewich et al., 2012; Moudén and Forbes, 2014; Lo et al., 2015; Holstein-Rathlou et al., 2016). Superimposed on the DE2 tide’s structure are regions of increasing and decreasing amplitudes, which may be the result of the constructive and destructive interference between DE2 and DW4, which is the most likely westward propagating tide. (This DE2 and DW4 interaction is also clear in MY33; see Figure S4.) Analysis of the phase tilts with height in Figure 5f, as well as in other years, suggests vertical wavelengths of $\sim 3H$ for the westward-traveling wave and $\sim 9H$ for the eastward-traveling wave (where H is the atmospheric scale height, with each decade

of pressure $\sim 2.3H$), which are in agreement with the expected wavelengths for the DE2 and DW4 tides (Wilson, 2000; Hinson and Wilson, 2004; Moulden and Forbes, 2014; Guzewich et al., 2012). See Forbes et al. (2020) for typical vertical wavelengths of tides based on classical theory. The phase structure near the surface is in agreement with the phase of the $s = 3$ component of topography.

The two eastward-propagating tides, DE1 and DE2, play a large role in shaping the nighttime cloud distribution seen in Figure 4b. At 3:35 am there is a region of clouds centered at $\sim 90^\circ\text{W}$, which extends from the surface to ~ 1 Pa and is tilted slightly eastward with height. There is a similar region in the eastern hemisphere, though cloud opacities are slightly lower here. These cloud regions occur at longitudes where the DE1 and DE2 tides constructively interfere to decrease nighttime temperatures. Elsewhere, temperatures remain too warm, resulting in the cloud-free regions. Where clouds form, local radiative cooling will lead to further decreases in temperature, and possibly further cloud formation, resulting in a positive feedback. This increased nighttime cooling due to clouds is partly responsible for the phase shift between 1–50 Pa in Figure 5e, which does not correlate with the expected vertical propagation of the surface-forced DE1 tide. Another factor contributing to the phase shift is the anti-symmetric component of the tide (not shown) which tilts eastward with height and has a vertical wavelength of $\sim 6.5H$, corresponding to the first anti-symmetric component of DE1 (Forbes et al., 2020). The anti-symmetric component is weaker than the symmetric component, but its phase is shifted $\sim 60^\circ$ to the east compared to the symmetric component.

The nighttime clouds located at $\sim 90^\circ\text{W}$ have larger opacities than those at $\sim 90^\circ\text{E}$. One reason for this is likely due to the global atmospheric circulation. Stationary waves play a large role in the transport of water away from the subliming north polar ice cap, and the stationary waves over the Tharsis region around southern hemisphere spring equinox tend to transport humid air southwards, while those in the Arabia Terra/Isidis region tend to transport drier air northwards (Steele et al., 2014). As such, the Tharsis region generally has larger water vapor abundances (Smith, 2002, 2004; Maltagliati et al., 2011; Wolkenberg et al., 2011; Trokhimovskiy et al., 2015), and hence clouds are likely to be more abundant. Another factor may be the effects of the D0 tide, which results in cooler nighttime temperatures due to the higher topography of the Tharsis region (Banfield et al., 2003; Guzewich et al., 2012).

In terms of the T_{ave} field, the phase structure of the $m = 1$ component suggests the presence of a tide with a westward phase tilt with height (Figure 5a), with a vertical wavelength of $\sim 7H$, possibly SW3. The $m = 2$ component of T_{ave} (Figure 5b) is less organized, and the changing amplitudes and phases with height suggest interference between eastward and westward propagating tides. Analysis of the phase tilts with height in other years, and at other latitudes in the tropics, suggests the westward- and eastward-propagating tides have vertical wavelengths of $\sim 2.5H$ and $\sim 4H$ respectively. It is not possible to identify the exact tides present, but the most likely are S0 and SW4. Lo et al. (2015) previously found evidence for S0 in upper-atmosphere MAVEN observations in mid latitudes. The larger amplitudes between 10–30 Pa may be the result of the radiative cooling associated with the nighttime clouds seen in Figure 4b. The $m = 3$ component of T_{ave} (Figure 5c) shows a barotropic structure above ~ 10 Pa. This is likely the SE1 tide, which has previously been observed in both the middle atmosphere (Guzewich et al., 2012) and upper atmosphere (Wilson, 2002; Wang et al., 2006; Lo et al., 2015).

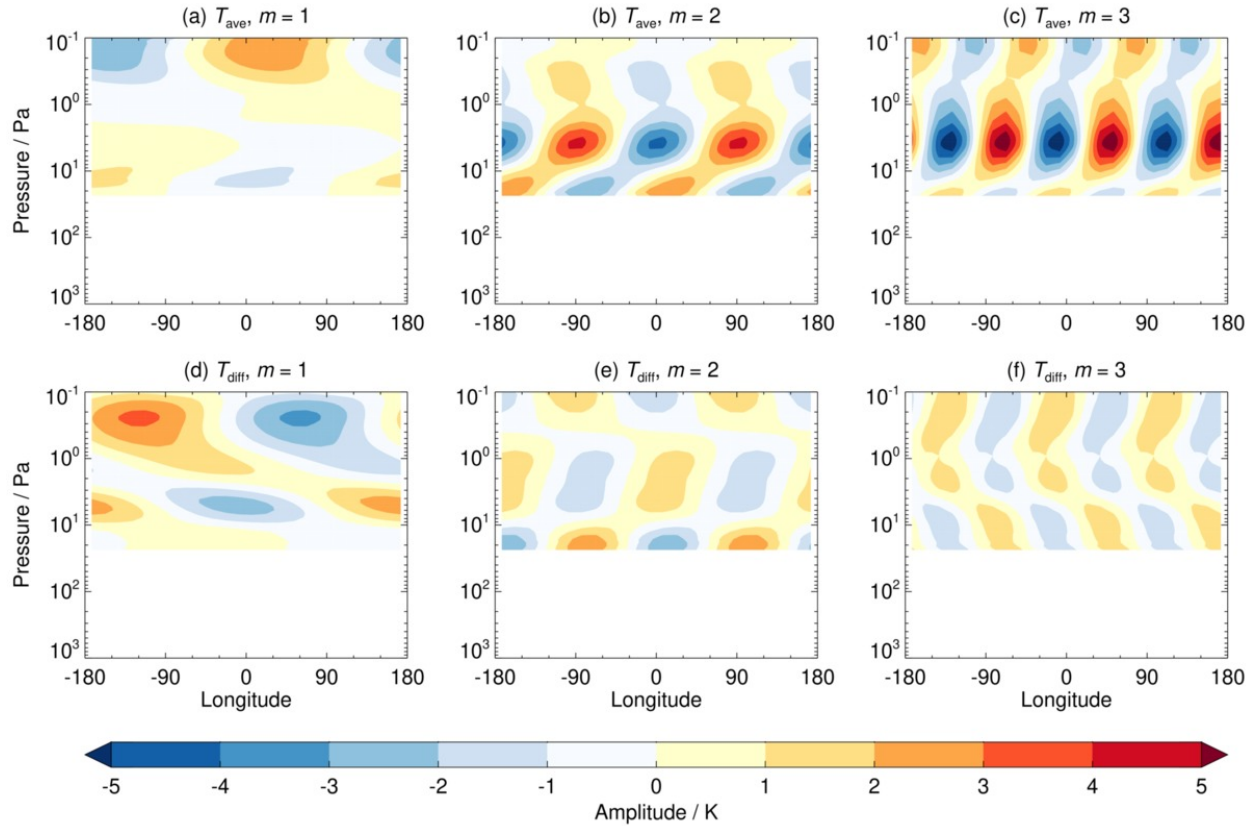


Figure 6: As Figure 5, but for MY30 cross-track data at a local time of 5:00 am/pm.

3.2.2 MY30 cross-track data

Figure 6 shows tide amplitudes and phases in the same format as Figure 5, but for MY30 cross-track measurements at a local time of $\sim 5:00$ am/pm. As noted earlier, the amplitudes of the $m = 2$ and $m = 3$ components of T_{ave} (Figure 6b,c), and the $m = 1$ component of T_{diff} (Figure 6d) increase when moving from 03:35 am to 05:00 am, and resemble those in MY29. The corresponding nighttime temperature and water ice distributions are shown in Figure 4c.

At altitudes below 10 Pa, the $m = 2$ component of T_{ave} shows a slight amplification of the tide structure that was present in the in-track data (compare Figures 5b and 6b). This may be from sampling the same tide at a different phase (due to the ~ 1.5 hour time difference), but the increased amplitudes also correlate with the regions of increased nighttime cloud abundance in Figure 4c. Thus, there may also be a contribution from local radiative cooling. Between ~ 1 –10 Pa, there is a region of large amplitudes that appear in the cross-track data, but are absent in the in-track data (peak amplitudes are ~ 5 K at ~ 4 Pa). This region shows a $\sim 90^\circ$ phase shift compared to the tide structure below. Comparing with Figure 4c, this region of increased amplitudes corresponds to the appearance of nighttime temperature inversions below ~ 5 Pa.

The vertical structure of the temperature inversions is shown in Figure 7, where temperature profiles from three different longitude regions between $L_S = 185$ – 190° are plotted. (Figure S5 shows the locations

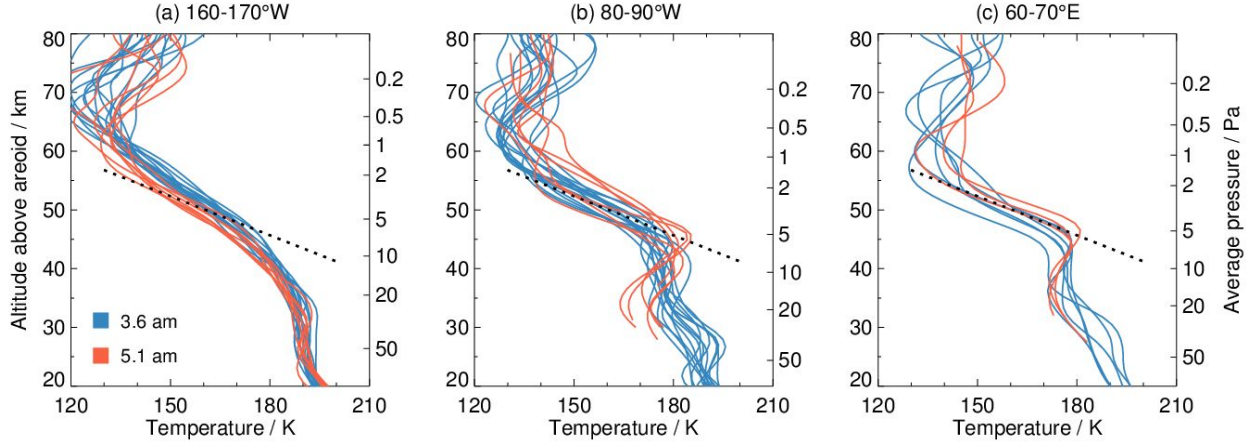


Figure 7: MY30 temperature profiles at 03:35 am (blue) and 05:00 am (red), from three different longitude regions. Data are averaged between 0–10°N and $L_S = 185\text{--}190^\circ$. The dashed black lines show the adiabatic temperature gradient $g/c_p = 4.5 \text{ K km}^{-1}$.

of all detected tropical temperature inversions.) Figure 7a shows profiles from a region where there are no large temperature inversions below $\sim 1 \text{ Pa}$, and there is little change in the temperature structure between 03:35 am and 05:00 am. In the 80–90°W and 60–70°E regions (Figure 7b,c), temperatures below $\sim 10 \text{ Pa}$ ($\sim 40 \text{ km}$) have cooled between 03:35 am and 05:00 am, likely due to cloud radiative effects (Hinson et al., 2014), with greater cooling at 80–90°W where clouds are thicker. Above the tops of the inversions (above $\sim 5 \text{ Pa}$), the temperatures can be seen to closely follow the adiabatic lapse rate, whereas this is not the case at 160–170°W, where no inversions occur. The local cooling by clouds, with associated warming above, suggests the increased temperatures are the result of adiabatic warming due to downwelling, with stronger downwelling and increased warming in regions with thicker clouds. This was confirmed via analysis of Ensemble Mars Atmosphere Reanalysis System data (see Appendix A). This area of adiabatic warming above the cooling cloud region is the reason for the 90° phase shift at $\sim 10 \text{ Pa}$ seen in Figures 6b and 6e.

In terms of the $m = 3$ component of T_{ave} , the phases are essentially the same in the in-track and cross-track measurements (compare Figures 5c and 6c), but the peak amplitude has increased from $\sim 3 \text{ K}$ to $\sim 6 \text{ K}$ between 3:35 am and 05:00 am. This suggests the presence of the same tide as before, SE1, with the larger amplitude the result of sampling the tide at a different phase. The $m = 1$ component of T_{diff} (Figure 6d) shows increased amplitudes between $\sim 3\text{--}8 \text{ Pa}$ that appear associated with a westward-tilted tide, with a vertical wavelength of $\sim 3.5H$. This is in agreement with the expected structure of the DW2 tide (Guzewich et al., 2012). The increased amplitudes correspond to a region of increasing cloud abundance, so there is again likely a contribution from cloud radiative effects. The remaining fields (the $m = 1$ component of T_{ave} and the $m = 3$ component of T_{diff}) do show changes to the tide structure between the in-track and cross-track data, but no large amplitude tides appear, and as such we do not discuss these components further.

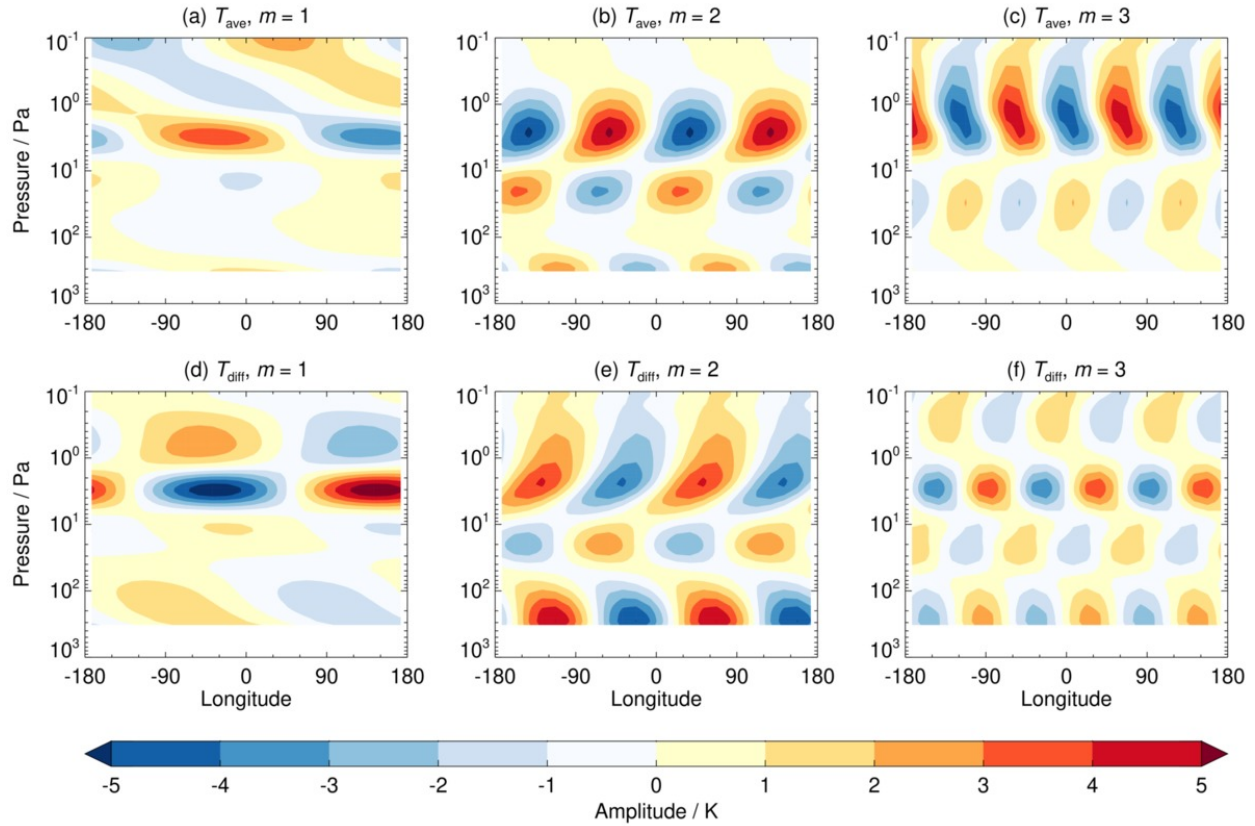


Figure 8: As Figure 5, but for MY29 in-track data at a local time of 3:45 am/pm.

3.2.3 MY29 in-track data

Comparing Figures 4b–d, the MY29 nighttime temperature and water ice distributions at 03:45 am more closely resemble the MY30 05:00 am data, as opposed to the MY30 03:35 data, despite the latter being closer in local time. As the temperature and ice distributions are largely influenced by diurnal tides, this suggests the early dust activity in MY29 has shifted the phase of the diurnal tide to an earlier local time. Such a shift, as a response to increased dustiness during global dust storms, has been noted previously in modeling and observations (e.g. Wilson and Richardson, 2000; Guzewich et al., 2016). However, the early dust activity in MY29 did not produce large dust optical depths like those experienced in global dust storms.

The amplitudes and phases of the tides in MY29 between $L_S = 180\text{--}200^\circ$ are shown in Figure 8. There is a general eastwards shift in the $m = 2$ and $m = 3$ tide phases compared to MY30 (Figure 5), which results in the clouds in Figure 4d being located further east than in MY30 (Figure 4b,c). This phase shift corresponds to an increase in the dust abundance of the low-lying planitias, which shifts the largest column dust opacities eastward between $L_S = 150\text{--}170^\circ$. The dust distribution then remains steady until $L_S = 200^\circ$, and correspondingly the tide phases show little change during this time. There is also an increase in the amplitudes of the westward-propagating tide components. These were most prominent after the onset of the early dust activity, but began to decrease in amplitude between $L_S = 150\text{--}170^\circ$ as the dust lofted by the

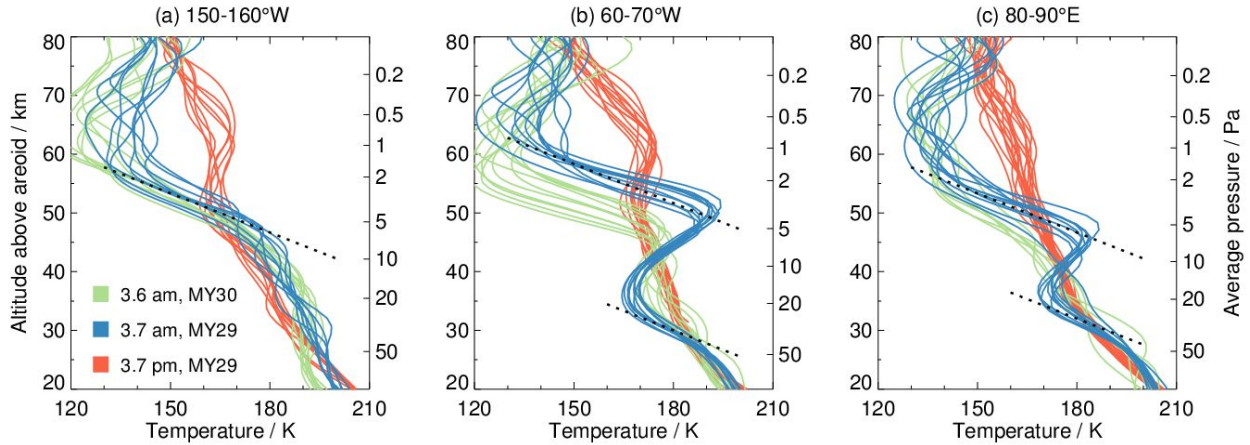


Figure 9: Temperature profiles from MY30 nighttime (green), MY29 nighttime (blue), and MY29 daytime (red) in-track measurements. Data are shown for three different longitude regions, and are averaged between $0\text{--}10^\circ\text{N}$ and $L_S = 190\text{--}195^\circ$. The dashed black lines show the adiabatic temperature gradient.

storm began decreasing in altitude. Despite this eastward shift, the tide structure in MY29 below ~ 10 Pa generally resembles that in the MY30 in-track data (Figure 5).

As in the MY30 cross-track data, nighttime temperature inversions occur in MY29, but these are much stronger than those in MY30, particularly in the western hemisphere. Figure 9 shows individual temperature profiles from three different longitude regions between $L_S = 190\text{--}195^\circ$, when the inversions are strongest. (Figure S6 shows the locations of all detected tropical temperature inversions.) Data are shown from 03:35 am in MY30, and 03:45 am/pm in MY29. The daytime temperatures are similar in all three regions, as are the nighttime temperatures above ~ 1 Pa. In Figure 9a, where no large temperature inversions occur below ~ 1 Pa, the nighttime temperatures in MY29 and MY30 are generally similar. In the $60\text{--}70^\circ\text{W}$ region, which has the strongest inversions (Figure 9b), the nighttime temperatures increase by ~ 25 K while ascending from 35–50 km. The coolest temperatures at the base of the inversions at 35 km are ~ 20 K cooler compared to the $150\text{--}160^\circ\text{W}$ region, and the warmest temperatures at 50 km are ~ 25 K warmer. The $80\text{--}90^\circ\text{E}$ region has weaker temperature inversions (Figure 9c), with peak temperatures occurring at ~ 45 km, compared to ~ 50 km at $60\text{--}70^\circ\text{W}$.

As in the MY30 cross-track data at 05:00 am (Figure 7), temperatures closely follow the adiabatic lapse rate above the tops of the inversions, suggesting adiabatic warming due to downwelling. However, the temperature inversions are much stronger in MY29 than in MY30, which suggests the diurnal and semidiurnal tides have been strengthened in the regions with inversions. The diurnal and semidiurnal tides have been observed to strengthen during global dust storms (Leovy and Zurek, 1979; Zurek, 1980; Bridger and Murphy, 1998; Guzewich et al., 2016, 2019; Viúdez-Moreiras et al., 2019), while more recent studies have revealed the semidiurnal tide is prominent all year, and is influenced by the distribution of water ice clouds as well as dust (Kleinböhl et al., 2013; Guzewich et al., 2016; Haberle et al., 2019). Due to the increased coverage to lower altitudes compared to MY30 cross-track measurements, the temperatures below the bases of the inversions in MY29 can also be seen to follow the adiabatic temperature gradient

(Figure 9b,c), showing that this is a region of convective instability (Hinson et al., 2014). This instability may cause water vapor (as well as dust and any other constituents present) from lower in the atmosphere to be transported upwards, increasing the cloud opacity and further strengthening the local cooling, leading to a positive feedback.

The nighttime temperature inversions in MY29 begin to appear at $L_S \approx 145^\circ$, and they strengthen and expand longitudinally until $L_S \approx 200^\circ$ (see Figure S6), in tandem with a general warming of the atmosphere. The increasing temperatures and longitudinal spreading of the regions with temperature inversions suggest that dust is playing a role in their formation. The dust abundance rapidly increases after the onset of the early dust activity, but then the height of the dust top falls between $L_S \approx 150\text{--}170^\circ$, before slowly rising again after $L_S \approx 170^\circ$. This more slow rising is likely due to upwelling in the Hadley cells, as the twin Hadley cell structure moves equatorward from the onset of the dust activity at $L_S \approx 143^\circ$ to $L_S \approx 200^\circ$ (Steele et al., 2014). The increase in dust height and opacity will lead to a strengthening of the diurnal and semidiurnal tides, which can in turn impact the non-migrating thermal tides. The inversions begin to decline between $L_S \approx 200\text{--}210^\circ$, during which time the circulation changes from a twin Hadley cell structure with upwelling in the tropics to an equator-crossing Hadley cell.

As seen in Figure 2, apart from the $m = 3$ component of T_{ave} , the large amplitude tides in the tropics in MY29 are focused in the 2–5 Pa region, and biased to the northern tropics, suggesting the tides are linked to a similar forcing mechanism. Also, from the analysis of MY30 cross-track data at local times of 05:00 am/pm, when the ice cloud distribution is a good match for that in MY29, only the $m = 2$ and $m = 3$ components of T_{diff} show a large amplitude increase (Figure 3). This suggests that the dust distribution in MY29 is playing an important role in strengthening the tides. Indeed, water ice clouds have been shown to influence the semidiurnal tide (Kleinböhl et al., 2013), which plays a key role in the structure of the T_{ave} field. This is likely why the tides in the T_{ave} field show an increase with local time in MY30, as the ice cloud distribution changes over the ~ 1.5 hour period, whereas the dust does not. However, the T_{diff} field is affected mainly by the diurnal tide, which is known to be sensitive to local dust loading (Leovy and Zurek, 1979; Bridger and Murphy, 1998; Guzewich et al., 2016). This is likely why the T_{diff} field shows stronger tides in MY29 compared to MY30, as the atmospheric dust content was larger.

The $m = 1$ components of both T_{ave} and T_{diff} have peak amplitudes at $\sim 30\text{--}40^\circ\text{W}$. This corresponds to a region of low-lying topography to the east of the Tharsis plateau and south of Acidalia Planitia, but does not correlate to a region of high or low amplitudes in the $s = 1$ component of topography, ruling out surface forcing of the tides. However, this region is a favored location for equator-crossing dust storms (Cantor, 2007; Wang and Richardson, 2015; Shirley et al., 2020), and the early dust activity in MY29 occurred in this region. Due to the low-lying topography, the column dust abundances here are larger, resulting in a stronger forcing of the $m = 1$ components of the tide. The phase change at ~ 3 Pa is related to the nighttime warming associated with the stronger downwelling.

The tide structures in the $m = 2$ components of T_{ave} are similar to those in the MY30 cross-track data (Figure 6b,e). The eastward tilt in the T_{diff} field is from an anti-symmetric tidal mode (not shown), with a wavelength of $\sim 6H$. This is comparable to the first anti-symmetric component of DE1 (Forbes et al., 2020). This anti-symmetric component exists with a similar amplitude in all years, but in MY29 it constructively

interferes with the symmetric component, causing an amplification of the tide above 10 Pa. The large-amplitude tide in the $m = 3$ component of T_{ave} shows a westward phase tilt compared to MY30. The lower atmosphere shows evidence for a westward-propagating wave with a vertical wavelength of $\sim 3H$, possibly SW5, which may be interacting with SE1 and causing the observed tilt. The region of large amplitudes in the $m = 3$ component of T_{diff} , centered at ~ 3 Pa, appears to result from an amplification of the westward-propagating DW4 tide, a weakening of the eastward-propagating DE2 tide, or both.

4 Conclusions

The results of the Fourier analysis of MY29 in-track temperatures, at a local time of $\sim 03:45$ am/pm around southern hemisphere spring equinox, reveal large amplitude non-migrating tides in the tropics that are not present in any other Mars year observed by MCS. MY29 experienced early dust activity, beginning at $L_S \approx 143^\circ$, and the observed tides began to strengthen after this dust activity, reaching their largest amplitudes at $L_S \approx 190^\circ$. Comparisons between daytime and nighttime temperatures show that it is the nighttime temperature distribution that is most perturbed in MY29, with strong temperature inversions located at ~ 35 – 55 km in the 15 – 90° W and 75 – 110° E regions, though these regions expand eastward with time between $L_S = 185$ – 200° . Due to this observed longitudinal spreading with L_S , the temperature inversions in MY29 appear to be related not only to the topography, but also to the aerosol distribution.

While the temperature inversions and tides continue to strengthen until $L_S \approx 190^\circ$ in MY29, the early dust storm activity ceased at $L_S \approx 157^\circ$ (Wang and Richardson, 2015). The continued strengthening of the tropical tides, and the longitudinal expansion of the regions displaying temperature inversions, suggests that dust continued to be transported equatorward and vertically. This is plausible, as the twin Hadley cell circulation has its upwelling branch over the tropics during southern hemisphere spring equinox. Transport by the Hadley cell circulation, aided by thermal tides, has been suggested as a mechanism for dust entering the northern jet and encircling Mars during the MY34 global dust storm, which also occurred during southern hemisphere spring equinox (Gillespie et al., 2020).

When analyzing MCS cross-track data in other years, taken at later local times of $\sim 05:00$ am/pm, some stronger tides do appear, notably in the $m = 2$ and $m = 3$ components of T_{ave} , where the tide structures resemble those in MY29. The T_{ave} field can have contributions from stationary waves, but the phases and inferred vertical wavelengths seem to suggest that it is the semidiurnal non-migrating tides that are amplified at later local times. In the case of the $m = 3$ component of T_{ave} , the amplification is likely due to sampling the eastward-propagating SE1 tide at a different local time, with aerosols having little impact. For the $m = 2$ component of T_{ave} , the tide amplification appears to be related to the water ice cloud distribution. The radiative cooling associated with regions of higher-opacity nighttime clouds causes stronger downwelling of the air aloft, and increased adiabatic warming. The local cooling at cloud level and warming above results in the appearance of nighttime temperature inversions.

The nighttime cloud structure, which results in the strengthening of the semidiurnal tide, is itself strongly influenced by the diurnal non-migrating tides, particularly the combination of the eastward-propagating DE1 and DE2 tides. Where these tides constructively interfere to decrease nighttime temperatures, clouds preferentially form, leading to increased radiative cooling. Due to this cooling, the bases of the temperature

inversions are regions of convective instability, which could result in water vapor (as well as dust and any other constituents present) from lower in the atmosphere being transported upwards, increasing the cloud opacity and further strengthening the local cooling, leading to a positive feedback.

Comparing different Mars years and different local times, it appears as though the radiative influence of water ice clouds is impacting the semidiurnal non-migrating tides in MY29 (and other years), while the large-amplitude diurnal non-migrating tides in MY29 are influenced by the early dust activity. The dust in MY29 was concentrated mostly in the northern tropics, which explains why the large tide amplitudes are biased towards this region. The fact that nighttime temperature inversions occur at earlier local times in MY29 (03:45 am) compared to other years (05:00 am) suggests there was a shift in the phase of the diurnal tide to an earlier local time. Such a shift, as a response to increased dustiness during global dust storms, has been noted previously in modeling and observations (e.g. [Wilson and Richardson, 2000](#); [Guzewich et al., 2016](#)).

While the early dust activity in MY29 did not produce large dust optical depths like those experienced in global dust storms, the dust activity occurred at a time when there was upwelling over the tropics, associated with the Hadley circulation, enabling the dust to be transported to higher altitudes where it has a larger radiative influence. The warmer tropical temperatures associated with the dust led to a strengthening of the Hadley circulation (as determined from the increased temperatures in the polar warmings above both polar vortices), resulting in a positive feedback. Combined with this increased vertical transport of dust, southern hemisphere spring equinox is when the water vapor column abundances in the tropics reach their largest value over the year ([Smith, 2004](#); [Heavens et al., 2011](#); [Wolkenberg et al., 2011](#); [Steele et al., 2014](#); [Trokhimovskiy et al., 2015](#)). As such, water vapor is also available for transport, which can result in increased cloud formation, which in turn can impact the tidal structure through local radiative heating and cooling. The tide amplitudes and temperature inversion strengths in MY29 begin to decrease after $L_S \approx 190^\circ$, in combination with a decrease in the dustiness of the tropics, a change in the overturning circulation to an equator-crossing Hadley cell, and a decrease in the water vapor abundance.

A Temperature inversions in EMARS data

In order to test the hypothesis that downwelling associated with the diurnal tide can cause the temperature inversions observed in the MCS measurements, we use Ensemble Mars Atmosphere Reanalysis System (EMARS) version 1.0 data ([Greybush et al., 2019](#)) for MY29. This dataset results from the assimilation of MCS in-track temperature profiles using a Local Ensemble Transform Kalman Filter (LETKF; see [Hoffman et al., 2010](#); [Greybush et al., 2012](#); [Zhao et al., 2015](#)), and is freely available at <https://www.datacommons.psu.edu/commonswizard/MetadataDisplay.aspx?Dataset=6171>. Dust and water ice tracers are advected by the model winds, and are radiatively active. However, for dust there is a source/sink term in the boundary layer that relaxes the model column opacities towards the dust maps of [Montabone et al. \(2015\)](#). We use the ‘background’ files, which result from 1-hour forecasts initiated from the LETKF analyses, as the analysis files only contain state variables and hence provide no information on the aerosol distributions. We temporally interpolate the hourly data in each grid box to obtain values at the same local time at each longitude.

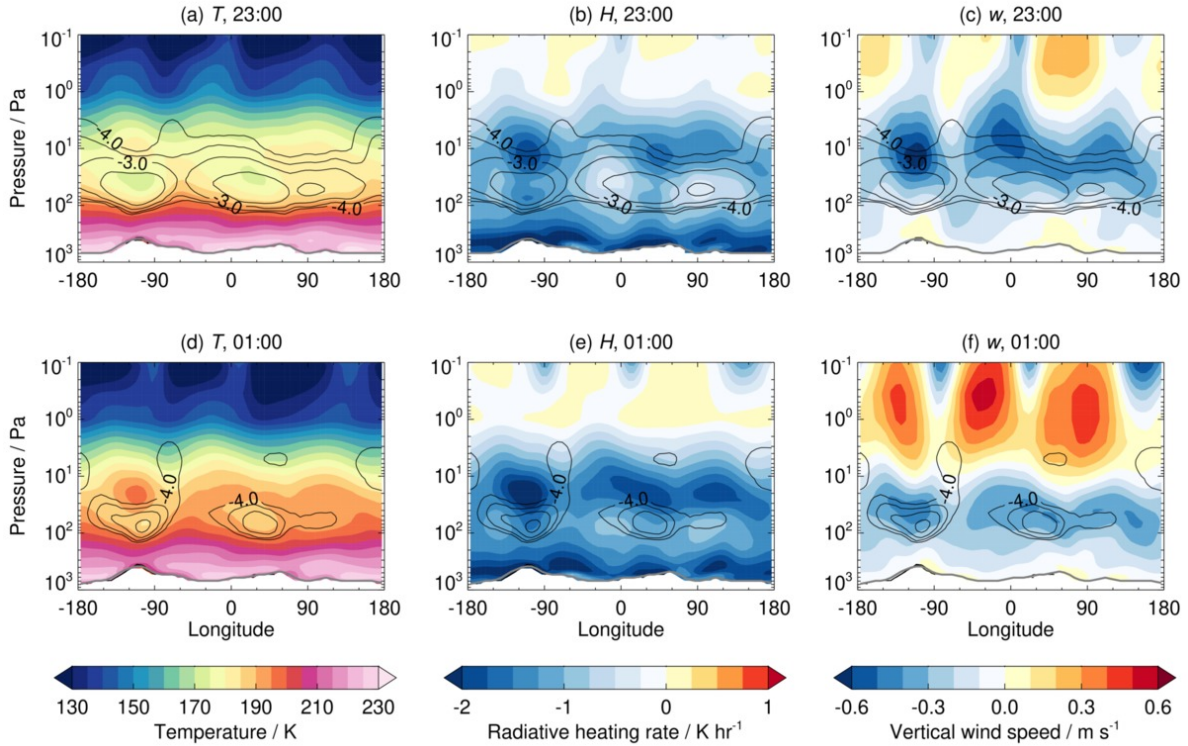


Figure A1: EMARS MY29 simulation results of (a,d) temperature, (b,e) radiative heating rate, and (c,f) vertical wind speed at 11:00 pm and 1:00 am. Data are averaged between $0\text{--}10^\circ\text{N}$ over $L_S = 180\text{--}200^\circ$. Black contours show water ice opacity per km in log units, in steps of 0.5.

Nighttime temperature inversions exist in the EMARS dataset in the $L_S = 180\text{--}200^\circ$ period, but they occur earlier in the night and lower in the atmosphere compared to the MCS data. The inversions begin forming at around $\sim 9:00$ pm, strengthen the most between 11:00 pm and 1:00 am, and disappear just after 3:00 am. The maximum temperature in the inversion over the Tharsis region increases by ~ 20 K between 11:00 pm and 1:00 am, while the temperature minima below the inversion increases by ~ 15 K. Figure A1 shows temperatures, radiative heating rates and vertical winds at 11:00 pm and 1:00 am. The heating rate is due to all gases and aerosols combined, as EMARS does not split the contributions from different species. It is clear that heating rates are negative everywhere below ~ 1 Pa, resulting in a cooling of the atmosphere. Thus, some other process must be responsible for the increased temperatures in the inversions. At this time the vertical wind speed, w , has negative values around the altitude of the inversions. This indicates downwelling in the atmosphere, and is strongest in regions with larger ice opacities. (Vertical winds were calculated from $\omega = dp/dt$, as output by EMARS, by assuming hydrostatic equilibrium.) The overall downward progression with time is associated with the diurnal tide, which is amplified by the radiative influence of clouds (Wilson and Richardson, 2000; Wilson and Guzewich, 2014). Due to compression of the air as it moves downwards, its temperature increases due to adiabatic warming (Hinson and Wilson, 2004; Wilson and Guzewich, 2014).

To investigate the potential warming caused by downwelling, we take the 11:00 pm temperatures, and

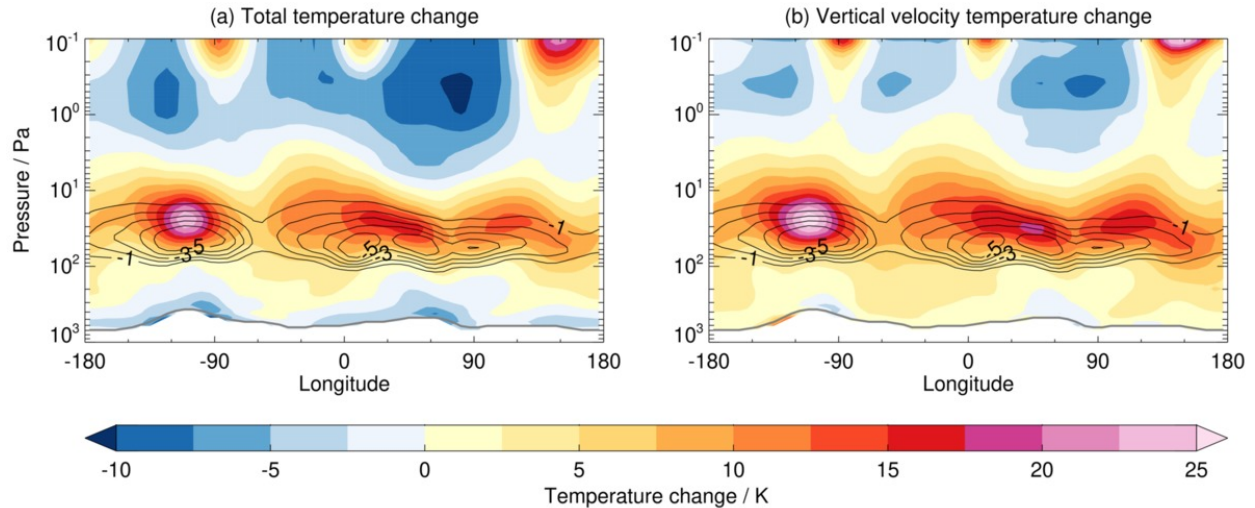


Figure A2: (a) Temperature change between 23:00 and 01:00 from EMARS MY29 simulation results, averaged between 0–10°N over $L_S = 180\text{--}200^\circ$. (b) Temperature change obtained by taking the 23:00 temperature and applying only the adiabatic dynamical heating from the vertical velocity. Black contours show the change in water ice opacity, in units of 10^{-3} km^{-1}

using only the adiabatic temperature changes caused by the vertical wind field (ignoring radiative heating or cooling) we calculate new temperatures in 5 minute intervals until 01:00 am. We do this at each grid point by using the vertical wind to determine the altitude of an air parcel 5 minutes earlier. We then interpolate the temperature profile to find the temperature at this location, T_{init} . Over the time interval Δt we then calculate the temperature change as $\Delta T = -w\Delta t g/c_p$, assuming a dry adiabatic lapse rate of $g/c_p = 4.5 \text{ K km}^{-1}$. The new temperature at the grid point is then $T_{\text{new}} = T_{\text{init}} + \Delta T$. The results, after two hours of iteration, are shown in Figure A2. As can be seen, most of the temperature changes that occur away from the surface between 11:00 pm and 1:00 am in the EMARS data can be attributed to the adiabatic heating or cooling of the air in response to the vertical winds. The temperature changes are slightly too large in the Tharsis region as radiative cooling is not taken into account. Between 3:00–5:00 am the vertical wind around the cloud layer becomes positive, and adiabatic heating ceases. Thus, it is likely that the large temperatures seen in the inversions in the MCS data are the result of increased downwelling due to stronger tides forced by cloud radiative effects.

Acknowledgements

The authors are grateful to Jeffrey Forbes for fruitful discussions about thermal tides, and to Sylvain Piqueux and Nicholas Heavens for helpful comments on the manuscript. The data used here are freely available from NASA’s Planetary Data System at https://atmos.nmsu.edu/data_and_services/atmospheres_data/MARS/mcs.html. This work was performed at the Jet Propulsion Laboratory, California Institute of Technology, under a contract with NASA. Copyright 2020, California Institute of Technology. Government sponsorship acknowledged.

References

- Banfield, D., Conrath, B., Pearl, J. C., Smith, M. D., and Christensen, P. (2000). Thermal tides and stationary waves on Mars as revealed by Mars Global Surveyor thermal emission spectrometer. *J. Geophys. Res.*, 105(E4):9521–9538.
- Banfield, D., Conrath, B. J., Smith, M. D., Christensen, P. R., and Wilson, R. J. (2003). Forced waves in the martian atmosphere from MGS TES nadir data. *Icarus*, 161(2):319–345.
- Bougher, S. W., Engel, S., Hinson, D. P., and Murphy, J. R. (2004). MGS Radio Science electron density profiles: Interannual variability and implications for the Martian neutral atmosphere. *J. Geophys. Res. (Planets)*, 109(E3):E03010.
- Bridger, A. F. C. and Murphy, J. R. (1998). Mars' surface pressure tides and their behavior during global dust storms. *J. Geophys. Res.*, 103(E4):8587–8602.
- Cahoy, K. L., Hinson, D. P., and Tyler, G. L. (2006). Radio science measurements of atmospheric refractivity with Mars Global Surveyor. *J. Geophys. Res. (Planets)*, 111(E5):E05003.
- Cantor, B. A. (2007). MOC observations of the 2001 Mars planet-encircling dust storm. *Icarus*, 186(1):60–96.
- Conrath, B. J. (1976). Influence of planetary-scale topography on the diurnal thermal tide during the 1971 Martian dust storm. *J. Atmos. Sci.*, 33:2430–2439.
- England, S. L., Liu, G., Withers, P., Yiğit, E., Lo, D., Jain, S., Schneider, N. M., Deighan, J., McClintock, W. E., Mahaffy, P. R., Elrod, M., Benna, M., and Jakosky, B. M. (2016). Simultaneous observations of atmospheric tides from combined in situ and remote observations at Mars from the MAVEN spacecraft. *J. Geophys. Res. (Planets)*, 121(4):594–607.
- Forbes, J. M. (1995). Tidal and Planetary Waves. *Washington DC American Geophysical Union Geophysical Monograph Series*, 87:67.
- Forbes, J. M. (2002). Wave Coupling in Terrestrial Planetary Atmospheres. *Washington DC American Geophysical Union Geophysical Monograph Series*, 130:171.
- Forbes, J. M. and Hagan, M. E. (2000). Diurnal Kelvin wave in the atmosphere of Mars: Towards an understanding of ‘stationary’ density structures observed by the MGS accelerometer. *Geophys. Res. Lett.*, 27(21):3563–3566.
- Forbes, J. M. and Miyahara, S. (2006). Solar Semidiurnal Tide in the Dusty Atmosphere of Mars. *J. Atmos. Sci.*, 63(7):1798–1817.
- Forbes, J. M., Zhang, X., Forget, F., Millour, E., and Kleinböhl, A. (2020). Solar Tides in the Middle and Upper Atmosphere of Mars. *J. Geophys. Res. Space Phys.*, 125(9).
- Gillespie, H. E., Greybush, S. J., and Wilson, R. J. (2020). An Investigation of the Encirclement of Mars by Dust in the 2018 Global Dust Storm Using EMARS. *J. Geophys. Res. (Planets)*, 125(7):e06106.
- Greybush, S. J., Kalnay, E., Wilson, R. J., Hoffman, R. N., Nehrkorn, T., Leidner, M., Eluszkiewicz, J., Gillespie, H. E., Wespetal, M., Zhao, Y., Hoffman, M. J., Dudas, P., McConnochie, T., Kleinböhl, A., Kass, D. M., McCleese, D. J., and Miyoshi, T. (2019). The Ensemble Mars Atmosphere Reanalysis System (EMARS) Version 1.0. *Geosci. Data J.*, 6(2):137–150.

- Greybush, S. J., Wilson, R. J., Hoffman, R. N., Hoffman, M. J., Miyoshi, T., Ide, K., McConnochie, T., and Kalnay, E. (2012). Ensemble Kalman filter data assimilation of Thermal Emission Spectrometer temperature retrievals into a Mars GCM. *J. Geophys. Res. (Planets)*, 117(E11):E11008.
- Guzewich, S. D., Lemmon, M., Smith, C. L., Martínez, G., de Vicente-Retortillo, Á., Newman, C. E., Baker, M., Campbell, C., Cooper, B., Gómez-Elvira, J., Harri, A. M., Hassler, D., Martin-Torres, F. J., McConnochie, T., Moores, J. E., Kahanpää, H., Khayat, A., Richardson, M. I., Smith, M. D., Sullivan, R., de la Torre Juárez, M., Vasavada, A. R., Viúdez-Moreiras, D., Zeitlin, C., and Zorzano Mier, M.-P. (2019). Mars Science Laboratory Observations of the 2018/Mars Year 34 Global Dust Storm. *Geophys. Res. Lett.*, 46(1):71–79.
- Guzewich, S. D., Newman, C. E., de la Torre Juárez, M., Wilson, R. J., Lemmon, M., Smith, M. D., Kahanpää, H., and Harri, A. M. (2016). Atmospheric tides in Gale Crater, Mars. *Icarus*, 268:37–49.
- Guzewich, S. D., Talaat, E. R., and Waugh, D. W. (2012). Observations of planetary waves and nonmigrating tides by the Mars Climate Sounder. *J. Geophys. Res. (Planets)*, 117(E3):E03010.
- Guzewich, S. D., Wilson, R. J., McConnochie, T. H., Toigo, A. D., Banfield, D. J., and Smith, M. D. (2014). Thermal tides during the 2001 Martian global-scale dust storm. *J. Geophys. Res. (Planets)*, 119(3):506–519.
- Haberle, R. M., Kahre, M. A., Hollingsworth, J. L., Montmessin, F., Wilson, R. J., Urata, R. A., Brecht, A. S., Wolff, M. J., Kling, A. M., and Schaeffer, J. R. (2019). Documentation of the NASA/Ames Legacy Mars Global Climate Model: Simulations of the present seasonal water cycle. *Icarus*, 333:130–164.
- Heavens, N. G., McCleese, D. J., Richardson, M. I., Kass, D. M., Kleinböhl, A., and Schofield, J. T. (2011). Structure and dynamics of the Martian lower and middle atmosphere as observed by the Mars Climate Sounder: 2. Implications of the thermal structure and aerosol distributions for the mean meridional circulation. *J. Geophys. Res. (Planets)*, 116(E1):E01010.
- Hinson, D. P., Asmar, S. W., Kahan, D. S., Akopian, V., Haberle, R. M., Spiga, A., Schofield, J. T., Kleinböhl, A., Abdou, W. A., Lewis, S. R., Paik, M., and Maalouf, S. G. (2014). Initial results from radio occultation measurements with the Mars Reconnaissance Orbiter: A nocturnal mixed layer in the tropics and comparisons with polar profiles from the Mars Climate Sounder. *Icarus*, 243:91–103.
- Hinson, D. P., Pätzold, M., Wilson, R. J., Häusler, B., Tellmann, S., and Tyler, G. L. (2008). Radio occultation measurements and MGCM simulations of Kelvin waves on Mars. *Icarus*, 193(1):125–138.
- Hinson, D. P. and Wilson, R. J. (2004). Temperature inversions, thermal tides, and water ice clouds in the Martian tropics. *J. Geophys. Res. (Planets)*, 109(E1):E01002.
- Hoffman, M. J., Greybush, S. J., John Wilson, R., Gyarmati, G., Hoffman, R. N., Kalnay, E., Ide, K., Kostelich, E. J., Miyoshi, T., and Szunyogh, I. (2010). An ensemble Kalman filter data assimilation system for the martian atmosphere: Implementation and simulation experiments. *Icarus*, 209(2):470–481.
- Holstein-Rathlou, C., Maue, A., and Withers, P. (2016). Atmospheric studies from the Mars Science Laboratory Entry, Descent and Landing atmospheric structure reconstruction. *Planet. Space Sci.*, 120:15–23.
- Jiang, F. Y., Yelle, R. V., Jain, S. K., Cui, J., Montmessin, F., Schneider, N. M., Deighan, J., Gröller, H., and Verdier, L. (2019). Detection of Mesospheric CO₂ Ice Clouds on Mars in Southern Summer. *Geophys. Res. Lett.*, 46(14):7962–7971.

- Joshi, M. M., Hollingsworth, J. L., Haberle, R. M., and Bridger, A. F. C. (2000). An interpretation of Martian thermospheric waves based on analysis of a general circulation model. *Geophys. Res. Lett.*, 27(5):613–616.
- Kass, D., Schofield, J., Kleinböhl, A., McCleese, D., Heavens, N., Shirley, J., and Steele, L. (2019). Mars Climate Sounder observation of Mars' 2018 global dust storm. *Geophys. Res. Lett.*
- Keating, G. M., Bougher, S. W., Zurek, R. W., Tolson, R. H., Cancro, G. J., Noll, S. N., Parker, J. S., Schellenberg, T. J., Shane, R. W., Wilkerson, B. L., Murphy, J. R., Hollingsworth, J. L., Haberle, R. M., Joshi, M., Pearl, J. C., Conrath, B. J., Smith, M. D., Clancy, R. T., Blanchard, R. C., Wilmoth, R. G., Rault, D. F., Martin, T. Z., Lyons, D. T., Esposito, P. B., Johnston, M. D., Whetzel, C. W., Justus, C. G., and Babicke, J. M. (1998). The Structure of the Upper Atmosphere of Mars: In Situ Accelerometer Measurements from Mars Global Surveyor. *Science*, 279:1672.
- Kleinböhl, A., Friedson, A. J., and Schofield, J. T. (2017). Two-dimensional radiative transfer for the retrieval of limb emission measurements in the martian atmosphere. *J. Quant. Spectrosc. Radiat. Transf.*, 187:511–522.
- Kleinböhl, A., John Wilson, R., Kass, D., Schofield, J. T., and McCleese, D. J. (2013). The semidiurnal tide in the middle atmosphere of Mars. *Geophys. Res. Lett.*, 40(10):1952–1959.
- Kleinböhl, A., Schofield, J. T., Abdou, W. A., Irwin, P. G. J., and de Kok, R. J. (2011). A single-scattering approximation for infrared radiative transfer in limb geometry in the Martian atmosphere. *J. Quant. Spectrosc. Radiat. Transf.*, 112:1568–1580.
- Kleinböhl, A., Schofield, J. T., Kass, D. M., Abdou, W. A., Backus, C. R., Sen, B., Shirley, J. H., Lawson, W. G., Richardson, M. I., Taylor, F. W., Teanby, N. A., and McCleese, D. J. (2009). Mars Climate Sounder limb profile retrieval of atmospheric temperature, pressure, and dust and water ice opacity. *J. Geophys. Res. (Planets)*, 114(E10):E10006.
- Kleinböhl, A., Spiga, A., Kass, D. M., Shirley, J. H., Millour, E., Montabone, L., and Forget, F. (2020). Diurnal Variations of Dust During the 2018 Global Dust Storm Observed by the Mars Climate Sounder. *J. Geophys. Res. (Planets)*, 125(1):e06115.
- Lee, C., Lawson, W. G., Richardson, M. I., Heavens, N. G., Kleinböhl, A., Banfield, D., McCleese, D. J., Zurek, R., Kass, D., Schofield, J. T., Leovy, C. B., Taylor, F. W., and Toigo, A. D. (2009). Thermal tides in the Martian middle atmosphere as seen by the Mars Climate Sounder. *J. Geophys. Res. (Planets)*, 114(E3):E03005.
- Leovy, C. B. (1981). Observations of Martian tides over Two annual cycles. *J. Atmos. Sci.*, 38:30–39.
- Leovy, C. B. and Zurek, R. W. (1979). Thermal tides and Martian dust storms: direct evidence for coupling. *J. Geophys. Res.*, 84:2956–2968.
- Leovy, C. B., Zurek, R. W., and Pollack, J. B. (1973). Mechanisms for Mars dust storms. *J. Atmos. Sci.*, 30:749–762.
- Lo, D. Y., Yelle, R. V., Schneider, N. M., Jain, S. K., Stewart, A. I. F., England, S. L., Deighan, J. I., Stiepen, A., Evans, J. S., Stevens, M. H., Chaffin, M. S., Crismani, M. M. J., McClintock, W. E., Clarke, J. T., Holsclaw, G. M., Lefèvre, F., and Jakosky, B. M. (2015). Nonmigrating tides in the Martian atmosphere as observed by MAVEN IUVS. *Geophys. Res. Lett.*, 42(21):9057–9063.

- Maltagliati, L., Titov, D. V., Encrenaz, T., Melchiorri, R., Forget, F., Keller, H. U., and Bibring, J.-P. (2011). Annual survey of water vapor behavior from the OMEGA mapping spectrometer onboard Mars Express. *Icarus*, 213(2):480–495.
- Mazarico, E., Zuber, M. T., Lemoine, F. G., and Smith, D. E. (2008). Observation of atmospheric tides in the Martian exosphere using Mars Reconnaissance Orbiter radio tracking data. *Geophys. Res. Lett.*, 35(9):L09202.
- McCleese, D. J., Schofield, J. T., Taylor, F. W., Calcutt, S. B., Foote, M. C., Kass, D. M., Leovy, C. B., Paige, D. A., Read, P. L., and Zurek, R. W. (2007). Mars Climate Sounder: An investigation of thermal and water vapor structure, dust and condensate distributions in the atmosphere, and energy balance of the polar regions. *J. Geophys. Res. (Planets)*, 112(E5):E05S06.
- Montabone, L., Forget, F., Millour, E., Wilson, R. J., Lewis, S. R., Cantor, B., Kass, D., Kleinböhl, A., Lemmon, M. T., Smith, M. D., and Wolff, M. J. (2015). Eight-year climatology of dust optical depth on Mars. *Icarus*, 251:65–95.
- Moudden, Y. and Forbes, J. M. (2008a). Effects of vertically propagating thermal tides on the mean structure and dynamics of Mars' lower thermosphere. *Geophys. Res. Lett.*, 35(23):L23805.
- Moudden, Y. and Forbes, J. M. (2008b). Topographic connections with density waves in Mars' aerobraking regime. *J. Geophys. Res. (Planets)*, 113(E11):E11009.
- Moudden, Y. and Forbes, J. M. (2010). A new interpretation of Mars aerobraking variability: Planetary wave-tide interactions. *J. Geophys. Res. (Planets)*, 115(E9):E09005.
- Moudden, Y. and Forbes, J. M. (2011). Simulated planetary wave-tide interactions in the atmosphere of Mars. *J. Geophys. Res. (Planets)*, 116(E1):E01004.
- Moudden, Y. and Forbes, J. M. (2014). Insight into the seasonal asymmetry of nonmigrating tides on Mars. *Geophys. Res. Lett.*, 41(7):2631–2636.
- Shirley, J. H., Kleinböhl, A., Kass, D. M., Steele, L. J., Heavens, N. G., Suzuki, S., Piqueux, S., Schofield, J. T., and McCleese, D. J. (2020). Rapid Expansion and Evolution of a Regional Dust Storm in the Acidalia Corridor During the Initial Growth Phase of the Martian Global Dust Storm of 2018. *Geophys. Res. Lett.*, 47(9):e84317.
- Smith, M. D. (2002). The annual cycle of water vapor on Mars as observed by the Thermal Emission Spectrometer. *J. Geophys. Res. (Planets)*, 107(E11):5115.
- Smith, M. D. (2004). Interannual variability in TES atmospheric observations of Mars during 1999-2003. *Icarus*, 167(1):148–165.
- Steele, L. J., Lewis, S. R., Patel, M. R., Montmessin, F., Forget, F., and Smith, M. D. (2014). The seasonal cycle of water vapour on Mars from assimilation of Thermal Emission Spectrometer data. *Icarus*, 237:97–115.
- Stevens, M. H., Siskind, D. E., Evans, J. S., Jain, S. K., Schneider, N. M., Deighan, J., Stewart, A. I. F., Crismani, M., Stiepen, A., Chaffin, M. S., McClintock, W. E., Holsclaw, G. M., Lefèvre, F., Lo, D. Y., Clarke, J. T., Montmessin, F., and Jakosky, B. M. (2017). Martian mesospheric cloud observations by IUVS on MAVEN: Thermal tides coupled to the upper atmosphere. *Geophys. Res. Lett.*, 44(10):4709–4715.

- Trokhimovskiy, A., Fedorova, A., Korablev, O., Montmessin, F., Bertaux, J.-L., Rodin, A., and Smith, M. D. (2015). Mars' water vapor mapping by the SPICAM IR spectrometer: Five martian years of observations. *Icarus*, 251:50–64.
- Viúdez-Moreiras, D., Newman, C. E., de la Torre, M., Martínez, G., Guzewich, S., Lemmon, M., Pla-García, J., Smith, M. D., Harri, A. M., Genzer, M., Vicente-Retortillo, A., Lepinette, A., Rodriguez-Manfredi, J. A., Vasavada, A. R., and Gómez-Elvira, J. (2019). Effects of the MY34/2018 Global Dust Storm as Measured by MSL REMS in Gale Crater. *J. Geophys. Res. (Planets)*, 124(7):1899–1912.
- Wang, H. and Richardson, M. I. (2015). The origin, evolution, and trajectory of large dust storms on Mars during Mars years 24-30 (1999-2011). *Icarus*, 251:112–127.
- Wang, L., Fritts, D. C., and Tolson, R. H. (2006). Nonmigrating tides inferred from the Mars Odyssey and Mars Global Surveyor aerobraking data. *Geophys. Res. Lett.*, 33(23):L23201.
- Wilson, R. J. (2000). Evidence for diurnal period Kelvin waves in the Martian atmosphere from Mars Global Surveyor TES data. *Geophys. Res. Lett.*, 27(23):3889–3892.
- Wilson, R. J. (2002). Evidence for nonmigrating thermal tides in the Mars upper atmosphere from the Mars Global Surveyor Accelerometer Experiment. *Geophys. Res. Lett.*, 29(7):1120.
- Wilson, R. J. and Guzewich, S. D. (2014). Influence of water ice clouds on nighttime tropical temperature structure as seen by the Mars Climate Sounder. *Geophys. Res. Lett.*, 41(10):3375–3381.
- Wilson, R. J. and Hamilton, K. (1996). Comprehensive model simulation of thermal tides in the Martian atmosphere. *J. Atmos. Sci.*, 53(9):1290–1326.
- Wilson, R. J. and Richardson, M. I. (2000). The Martian atmosphere during the Viking mission. I. Infrared measurements of atmospheric temperatures revisited. *Icarus*, 145(2):555–579.
- Withers, P., Bougher, S. W., and Keating, G. M. (2003). The effects of topographically-controlled thermal tides in the martian upper atmosphere as seen by the MGS accelerometer. *Icarus*, 164(1):14–32.
- Withers, P., Pratt, R., Bertaux, J. L., and Montmessin, F. (2011). Observations of thermal tides in the middle atmosphere of Mars by the SPICAM instrument. *J. Geophys. Res. (Planets)*, 116(E11):E11005.
- Wolkenberg, P., Smith, M. D., Formisano, V., and Sindoni, G. (2011). Comparison of PFS and TES observations of temperature and water vapor in the martian atmosphere. *Icarus*, 215(2):628–638.
- Wu, Z., Li, T., and Dou, X. (2015). Seasonal variation of Martian middle atmosphere tides observed by the Mars Climate Sounder. *J. Geophys. Res. (Planets)*, 120(12):2206–2223.
- Wu, Z., Li, T., and Dou, X. (2017). What causes seasonal variation of migrating diurnal tide observed by the Mars Climate Sounder? *J. Geophys. Res. (Planets)*, 122(6):1227–1242.
- Zhao, Y., Greybush, S. J., Wilson, R. J., Hoffman, R. N., and Kalnay, E. (2015). Impact of assimilation window length on diurnal features in a Mars atmospheric analysis. *Tellus A*, 67(1):26042.
- Zurek, R. W. (1976). Diurnal tide in the Martian atmosphere. *J. Atmos. Sci.*, 33:321–337.
- Zurek, R. W. (1980). Surface pressure response to elevated tidal heating sources: comparison of Earth and Mars. *J. Atmos. Sci.*, 37:1132–1136.
- Zurek, R. W. (1988). Free and forced modes in the Martian atmosphere. *J. Geophys. Res.*, 93:9452–9462.

Zurek, R. W. and Leovy, C. B. (1981). Thermal Tides in the Dusty Martian Atmosphere: A Verification of Theory. *Science*, 213(4506):437–439.